Published in final edited form as:
Neuroimage. 2008 April 15; 40(3): 1130–1143.

A Novel Technique for Modeling Susceptibility-Based Contrast Mechanisms for *Arbitrary* Microvascular Geometries: The Finite Perturber Method

Arvind P. Pathak[1], **B. Douglas Ward**[2], and **Kathleen M. Schmainda**[2,3]

1 *JHU ICMIC Program, Russell H. Morgan Department of Radiology and Radiological Science and Department of Oncology, The Johns Hopkins University School of Medicine, Baltimore, MD*

2 *Department of Biophysics, Medical College of Wisconsin, Milwaukee, WI*

3 *Department of Radiology, Medical College of Wisconsin, Milwaukee, WI*

Abstract

Recently, we demonstrated that vessel geometry is a significant determinant of susceptibility-induced contrast in MRI. This is especially relevant for susceptibility-contrast enhanced MRI of tumors with their characteristically abnormal vessel morphology. In order to better understand the biophysics of this contrast mechanism, it is of interest to model how various factors, including microvessel morphology contribute to the measured MR signal, and was the primary motivation for developing a novel computer modeling approach called the Finite Perturber Method (FPM). The FPM circumvents the limitations of traditional fixed-geometry approaches, and enables us to study susceptibility-induced contrast arising from *arbitrary* microvascular morphologies in 3D, such as those typically observed with brain tumor angiogenesis. Here we describe this new modeling methodology and some of its applications. The excellent agreement of the FPM with theory and the extant susceptibility modeling data, coupled with its computational efficiency demonstrates its potential to transform our understanding of the factors that engender susceptibility contrast in MRI.

Keywords

Dynamic susceptibility; contrast; arbitrary geometry; microvasculature; tumor angiogenesis; BOLD fMRI

INTRODUCTION

In 1990, Rosen et al (Rosen, 1990) demonstrated that if a bolus of a high dose of gadolinium (Gd)-chelated contrast agent was administered and MR images acquired rapidly during this administration, a transient decrease in signal intensity was observed. This transient signal decrease could then be converted into a concentration-time curve, from which the relative cerebral blood volume (rCBV) could be computed for each image voxel using tracer kinetic principles (Zierler, 1962). This imaging approach was based on the principle of susceptibility-induced contrast. Specifically, if a high concentration of a paramagnetic contrast agent such

Address for Correspondence: Kathleen M. Schmainda, Ph.D., Dept. of Biophysics, Medical College of Wisconsin, 8701, Watertown Plank Rd., Milwaukee, WI 53226, U. S. A. Tel: (414) 456-4051, Fax: (414) 456-6512, E-mail: kathleen@mcw.edu.

as a Gd-chelate or a superparamagnetic iron-oxide contrast agent such as MION (Shen, 1993) is confined to the vascular space, a difference in susceptibility or "magnetizability" between the vessel and tissue arises. Water protons diffusing through this resulting magnetic field gradient lose phase coherence, inducing a transient decrease in the MR signal intensity proportional to the fractional blood volume within the imaging voxel. The development of dynamic susceptibility contrast (DSC) MRI enabled differentiation between gray and white matter (Rosen, 1991a), made functional MR imaging (fMRI) of brain activation possible (Belliveau, 1991), with several laboratories eventually demonstrating the feasibility of using DSC techniques for determining the rCBV in patients with brain tumors (Aronen, 1994; Donahue et al., 2000; Maeda, 1993).

However, implicit in all the abovementioned DSC studies is the assumption that the relationship between the measured MR signal (i.e. change in T2 or T2* relaxation rate) and contrast agent concentration, which is characterized by the susceptibility calibration factor, is the same for normal brain and tumor tissue (Rosen, 1991b). Recent work by Pathak et al challenged this assumption, revealing a different susceptibility calibration factor for brain and tumor tissue in a rat brain tumor model (Pathak et al., 2003). It was demonstrated that this difference in susceptibility calibration factors was not explicable by differences in the fractional vascular volumes, but was probably due to the grossly different vascular morphology of brain tumors compared to healthy brain tissue. Tumor vessels are characteristically more sinusoidal and tortuous than normal brain vessels, especially at advanced stages of growth (Pathak et al., 2001). Furthermore, these observations were consistent with results of simulations conducted by Boxerman et al (Boxerman JL, 1993), which showed that susceptibility relationships were different for spherical versus cylindrical perturbers, and more recently with analysis by Kiselev showing differences between the arterial and tissue susceptibility relationship (Kiselev, 2001).

Consequently, to use susceptibility-based techniques more appropriately, such as DSC to evaluate pathologies, we need a better understanding of susceptibility relationships under pathologic conditions. An important approach in this regard is to use models to simulate susceptibility relationships under various conditions, e.g. contrast agent dose, vessel diameters, blood volumes etc. However, most current susceptibility contrast models assume a specific perturber geometry for representing the microvessel architecture of the tissue being studied. These have included the use of a single cylinder (Bandettini, 1995; Ogawa, 1990), multiple cylinders (Fisel, 1991; Kennan, 1994), spherical perturbers (Weisskoff, 1994), and ensembles of randomly oriented cylinders (Boxerman, 1995a; Yablonskiy, 1994), and have provided invaluable insights into susceptibility contrast mechanisms. Nonetheless, cylindrical or spherical perturbers may not adequately represent the anomalous vascular morphology of tumors. Additionally, the cylindrical perturber (CP) approaches assume that the magnetic field does not vary along the length of the vessel, thus allowing these effects to be simulated in 2D. However, any vessel geometry that departs from the cylindrical model would need to be simulated in 3D, since the microscopic magnetic field gradients are a function of the 3D geometry. In addition, some CP models assume large inter-vessel separation, so that effects of overlapping field gradients may be ignored. This assumption may be inappropriate for tumors, for which vessel density can be either high or low, but with larger caliber tumor vessels, such that the inter-vessel distance may not be negligible (Deane, 1981). Further, overlapping field gradients may become significant at high contrast agent doses and dominate the eventual image contrast. As a result, the primary goal of this study was to develop a computer model that could simulate susceptibility-based contrast for arbitrary microvessel geometries while employing the *de facto* capillary geometry from the rat cortex as an input to this model.

While there have been several approaches developed for calculating the field for arbitrary geometries that include both non-Fourier (Li and Leigh, 2004) and Fourier approaches

(Jenkinson et al., 2004; Koch et al., 2006), we independently proposed the finite perturber method (FPM) technique (Pathak, 2002). Although analogous, the Jenkinson and Koch approaches differ in both, methodology and application from the present paper. Namely, they were concerned with the estimation and correction of field distortions due to inhomogeneous magnetic fields, which produce MR image artifacts. The results presented therein-modeled field distortion at the level of the whole-brain. However, our FPM approach is specifically geared towards modeling susceptibility-induced field perturbations arising at the microvascular (i.e., sub-voxel) level, producing the image contrast of interest. Furthermore, we employ the estimated magnetic field perturbations to calculate the MR signal itself by simulating proton diffusion and phase accumulation. The FPM circumvents the limitations of traditional fixed-geometry approaches, and enables us to study susceptibility-induced contrast arising from *arbitrary* microvascular morphologies, such as those that typically result from tumor angiogenesis. In this paper, we describe this new modeling methodology and some of its applications.

METHODS

In this section, we first describe the numerical technique, which we refer to as the Finite Perturber Method (FPM), for calculating the magnetic field shifts arising from an arbitrary microvascular geometry having a given magnetic susceptibility difference from the surrounding tissue. Second, we validate the FPM by comparing its performance with that predicted by theoretical solutions for perturbers with simple geometries, and extant modeling data on the vessel size dependence of the gradient- and spin-echo relaxation rates. Finally, we present an illustration of the FPM calculated MR signal for the microvascular architecture of the rat cortex using susceptibility differences characteristic of the blood oxygenation level dependent (BOLD) contrast mechanism.

General Description of the Finite Perturber Model (FPM)

The Finite Perturber Method (FPM) differs from classical numerical methods for computing electrical or magnetic fields such as the Finite Difference Method (FDM) and the Finite Element Method (FEM) in that it does not attempt to solve Maxwell's equations directly. Instead, the vascular structure for which the magnetic field changes need to be computed is represented by numerous small "perturbers". To calculate the magnetic field shift at a given point, the contribution to the magnetic field shift due to each perturber is calculated independently. The total magnetic field shift is then evaluated as the sum of the magnetic field shifts from all of the perturbers. In the most general case, a simple summation of the magnetic field shifts would not suffice because there would be interactions among the perturbers. However, for the present application, this effect can be ignored as typical main magnetic field strengths (B_0) range from 1–3 Tesla, whereas the magnetic field shifts that give rise to susceptibility-based contrast are on the order of $B = 10^{-6}$ Tesla. Therefore, the effect of such inter-perturber interactions is negligible, and treating perturbers as if they are acting independently is justified.

We implemented the FPM as a program in Matlab®. The inputs to the FPM computational engine are: a tabular listing of the vascular structure; the B_0 field components; the susceptibility difference ($\Delta\chi$) between the vasculature and surrounding tissue; the echo time (TE) to use in calculating the MR signal; the number of protons to use in the Monte Carlo simulation; and the diffusion coefficient (D). The FPM then generates the following: (1) a 3D "anatomical" data structure representing the vasculature or substrate upon which all subsequent computations are conducted. (2) A 3D "functional" dataset of the magnetic field perturbations arising from the entire vascular substrate, and (3) modeling of proton diffusion and subsequent computation of the evolution of the MR signal over time. A description of each of these modules follows.

Generating the Anatomical Data Structure

The anatomical substrate for our simulations was a digitized 3D representation of a cerebrocortical capillary network (≈320μm×320μm×70μm) obtained from a rat cortex (Hudetz, 1993). Briefly, optical sectioning light microscopy was employed to trace out the X, Y, and Z coordinates of various vessel segments obtained from a microvascular corrosion cast of the rat cerebral cortex. The X and Y coordinates of the vessels were digitized directly off the computer monitor, while Z coordinates were obtained from a potentiometer attached to the focusing knob of the microscope that kept track of the depth of focus. The vessel segment radius was also measured at each stage. The resultant data structure was a tabular listing, wherein each vessel was represented as a sequence of short, connected cylindrical segments with the centers of the two circular faces of each segment specified by a set of (x, y, z) coordinates, and radius r of the cylindrical segment connecting the two faces. To avoid gaps in the structural representation, a hemisphere of the same radius capped each circular face of the cylindrical section. The FPM converts this input data structure into a 3D array of numbers representing the "anatomical" dataset. Typically, this is a binary array with "0" or a "1", corresponding either to points lying "outside" or "inside" the vascular structure, respectively. Since we use small, but finite, cubes in place of infinitesimal elements in our numerical approximation, and as the cubes have finite extent, they may lie completely inside the vasculature, completely outside, or part inside and part outside. It is for this reason that we allow the possibility of accounting for the fractional occupancy of a cube, in which case elements of the matrix representing the vascular structure may take on values between 0 and 1, inclusive. The option of employing the fractional occupancy function is especially relevant to cases wherein the vessel structure is much finer than the simulation cell size.

The above ("tree" to 3D array structure) reconstruction was necessary for the vascular trees obtained using our optical sectioning light microscopy method. However, it is important to point out that any high-resolution "binarized" 3D vascular tree dataset could be employed directly as the input anatomical substrate for the FPM, thereby obviating this processing step.

Computing the Magnetic Field Shift Due to the Vascular Structure

Our approach to modeling the magnetic field perturbation arising from an arbitrarily shaped vasculature was to "fill" it with numerous very small perturbers. To calculate the magnetic field shift due to our *finite perturber*, we consider a sphere to be embedded in the cube, as illustrated in Fig. 1a. The radius 'a' of the sphere is one-half the side length of the cube. The magnetic field shift, due to the sphere itself, at point **p**(x,y,z) at distance 'r' from the center, and at an angle θ with respect to $\mathbf{B}_0$, is given by (Haacke, 1999;Landau and Lifshitz, 1984):

$$\Delta B_{sphere}(x,y,z) = \frac{\Delta\chi}{3}\frac{a^3}{r^3}(3\cos^2\theta - 1)B_0 \quad (1)$$

However, we are using an ensemble of many finite perturbers to model the macroscopic effect of the vasculature. These perturbers are small, but due to computational limitations, are not infinitesimal. The problem with using spheres as the finite perturbers is that it is not possible to completely fill the vascular space using spheres of finite radius, because gaps would remain between the spheres. Therefore, we "filled" the vasculature with cubes of finite size using the following modification of Eq. 1. Since the volume of a cube is larger than the volume of the embedded sphere (by a factor of $\frac{6}{\pi}$), we can approximate the magnetic field shift due to the cube (i.e. the finite perturber) by:

$$\Delta B_{cube}(x,y,z) = \left(\frac{6}{\pi}\right)\frac{\Delta\chi}{3}\frac{a^3}{r^3}(3\cos^2\theta - 1)B_0 \quad (2)$$

From Eq. 2, we can see there is a $\frac{1}{r^3}$ dependence of the magnitude of ΔB_{cube} relative to '*r*'. Since this quantity falls off rapidly, the error introduced by a coarse approximation to the vascular structure at a (relatively) long distance from the test point **p** is negligible. However, for vasculature close to **p**, an accurate, high-resolution representation of the vasculature is required to minimize this error.

The above equation yields the magnetic field change (ΔB_{cube}) arising from a single finite perturber. To calculate the total magnetic field perturbation arising from the entire vasculature, we let the radius '*a*' of the finite perturber become infinitesimally small, and integrate over the entire simulation space:

$$\Delta B(x,y,z) = \iiint V(\xi,\eta,\zeta)\Delta B_{cube}(x-\xi, y-\eta, z-\zeta)d\xi d\eta d\zeta \tag{3}$$

Where V(x,y,z) is a binary function indicating whether a given point (x,y,z) lies within the vasculature, i.e.:

$$V(x,y,z) = \begin{cases} 1, if(x,y,z) is inside the vasculature, \\ 0, if(x,y,z) is outside the vasculature. \end{cases} \tag{4}$$

Now, Eq. 4 applies for this theoretical derivation, wherein the integrals are over infinitesimal elements. Hence, a particular point is either inside or outside the vasculature. However, in the numerical approximation to the vascular structure, as discussed earlier, we use small, but finite, cubes in place of these infinitesimal elements. Since these cubes have finite extent, they may lie completely inside the vasculature, completely outside, or part inside and part outside. It is for this reason that we included the possibility of estimating the fractional occupancy of a cube as follows: a number (say, *n*) of points are selected at random from each cell, and evaluated to determine whether they lie inside or outside the vasculature. For a particular cell in the simulation universe, if *k* of these random points is determined to lie inside the vasculature, the occupancy of that cell is estimated by the fraction *k/n*. Thus, cells that lie completely inside the vasculature have fractional occupancy of 1.0; those that lie completely outside the vasculature have fractional occupancy of 0.0; with elements of the matrix representing the vascular structure taking values between 0 and 1, inclusive. In all our simulations, except for those with the cerebrocortical capillary network, we employed the binary function (i.e. no intermediate values of fractional occupancy) when representing the vasculature.

Next, taking the 3D Fourier transform of both sides of Eq. 3 yields:

$$\Im\{\Delta B(x,y,z)\} = \Im\left\{\iiint V(\xi,\eta,\zeta)\Delta B_{cube}(x-\xi, y-\eta, z-\zeta)d\xi d\eta d\zeta\right\} \tag{5}$$

We can immediately recognize Eq. 5 as the Fourier transform of the 3D convolution of the vascular structure with the finite perturber field, which may be rewritten as:

$$\Im\{\Delta B(x,y,z)\} = \Im\{V(x,y,z) \otimes \Delta B_{cube}(x,y,z)\} \tag{6}$$

Since the Fourier transform of the convolution of two functions is equal to the product of the Fourier transforms of the individual functions, Eq. 6 becomes:

$$\Im\{\Delta B(x,y,z)\} = \Im\{V(x,y,z)\}\Im\{\Delta B_{cube}(x,y,z)\} \tag{7}$$

Taking the inverse Fourier transform of Eq. 7, gives:

$$\Delta B(x,y,z) = \Im^{-1}\{\Im\{V(x,y,z)\}\Im\{\Delta B_{cube}(x,y,z)\}\} \tag{8}$$

Now, Eq. 8 suggests a computationally efficient means of calculating the magnetic field perturbation map arising from the entire vasculature, by using the Fast Fourier Transform (FFT)

to perform the convolution. The general procedure for this reduces to the following steps: (1) Convert the input node-and-branch tabular representation of the vasculature into a 3D simulation grid. (2) Calculate the 3D magnetic field arising from a single finite perturber using Eq. 2. (3) Calculate the 3D FFT of the vascular structure. (4) Calculate the 3D FFT of the finite perturber field. (5) Perform a point-wise multiplication of the two 3D FFT's. (6) Calculate the inverse FFT of this product. Due to the computationally efficient nature of the FFT, these calculations can be performed in a few minutes. Steps 1–6 are illustrated in Fig. 2. The results for the reconstructed cerebrocortical capillary network of Fig. 1b are shown in Fig. 1c.

Computing the Magnetic Field Shift for Simple Geometries

It is possible to evaluate the accuracy of the numerical estimate of the magnetic field shift induced by a vessel represented by a few simple geometries, such as a sphere or infinite cylinder, in regions with different susceptibilities, since the theoretical solutions for the magnetic field shift inside and outside such geometries are known. While we have neglected terms involving the background tissue susceptibility, we do not assume that the susceptibility outside the vasculature is zero. It is the difference in susceptibility ($\Delta\chi$) between inside and outside the vasculature that is relevant as far as the de-phasing effect of the inhomogeneous magnetic field is concerned. To validate the numerical accuracy of the FPM, we compared the results obtained with the FPM with theoretical values of the magnetic field change for the following selected geometries:

(a) An infinite cylinder with B_0 perpendicular to its long axis—Suppose an infinite cylindrical perturber of radius 'a' is placed in a magnetic field B_0 such that the field is perpendicular to the axis of the cylinder, e.g. B_0 is along the z-axis and the cylinder axis along the y-axis as shown in Fig. 3a. If we examine the magnetic field shift along a line through the center of the cylinder, perpendicular to the axis, and parallel to the B_0 field, the theoretical field shift (including the Lorentz correction) is given by (Haacke, 1999;Landau and Lifshitz, 1984):

$$\Delta B = \begin{cases} -\frac{1}{6}\Delta\chi B_0 & inside the cylinder \\ \frac{1}{2}\Delta\chi\frac{a^2}{\rho^2}B_0 & outside the cylinder \end{cases} \quad (9)$$

where 'ρ' is the distance to the test point. For the same magnetic field and cylinder orientation, if we examine the magnetic field shift along a line through the center of the cylinder, perpendicular to the axis, but along a line perpendicular to the B_0 field, the theoretical field shift (including the Lorentz correction) is given by (Haacke, 1999;Landau and Lifshitz, 1984):

$$\Delta B = \begin{cases} -\frac{1}{6}\Delta\chi B_0 & inside the cylinder \\ -\frac{1}{2}\Delta\chi\frac{a^2}{\rho^2}B_0 & outside the cylinder \end{cases} \quad (10)$$

(b) An infinite cylinder with B_0 parallel to its long axis—We again consider an infinite cylindrical perturber; however, now the main B_0 field is *parallel* to the axis of the cylinder. If we examine the magnetic field shift along a line through the center of the cylinder, perpendicular to the axis, and thus perpendicular to the B_0 field, the theoretical field shift (including the Lorentz correction) is given by (Haacke, 1999; Landau and Lifshitz, 1984):

$$\Delta B = \begin{cases} \frac{1}{3}\Delta\chi B_0 & inside the cylinder \\ 0 & outside the cylinder \end{cases} \quad (11)$$

(c) Sphere—Consider a sphere of radius 'a', placed in a magnetic field B_0. If we examine the magnetic field shift along a line through the center of the sphere, parallel to B_0, the

theoretical field shift (including the Lorentz correction) is given by (Haacke, 1999; Landau and Lifshitz, 1984):

$$\Delta B = \begin{cases} 0 & inside the sphere \\ \frac{2}{3}\Delta\chi\frac{a^3}{\rho^3}B_0 & outside the sphere \end{cases} \quad (12)$$

If, on the other hand, we examine the magnetic field shift along a line through the center of the sphere, but perpendicular to the B_0 field, the theoretical field shift (including the Lorentz correction) is given by (Haacke, 1999; Landau and Lifshitz, 1984):

$$\Delta B = \begin{cases} 0 & inside the sphere \\ -\frac{1}{3}\Delta\chi\frac{a^3}{\rho^3}B_0 & outside the sphere \end{cases} \quad (13)$$

For all of the above scenarios we employed the following simulation parameters: B_0=1.5T and $\Delta\chi=4\pi\times(1-0.6)\times0.42\times0.18\times10^{-6}=3\times10^{-8}$, corresponding to BOLD contrast with 60% venous oxygenation and 42% hematocrit (Bandettini and Wong, 1995). For determining the effect of simulation grid size and therefore the number of finite perturbers on the accuracy of the FPM calculated magnetic field for scenario (a), we employed simulation grid sizes of 64×64×64, 128×128×128 and 256×256×256, while holding the fractional volume of the cylinder constant at ~2%. We then calculated the difference between the magnetic field computed from theory and the FPM field along three-orthogonal axes for each case.

Simulation of Proton Diffusion Effects and Estimation of the MR Signal

Simulation of proton diffusion is an important component of the MR signal calculation, since each individual proton "sees" a different magnetic field shift at different points along its trajectory. Proton diffusion was modeled using a Monte Carlo approach. Typically, thousands of "protons" are initially placed at random locations within the simulation space. Then, with each increment of the simulation time, each proton is moved from its previous position (x, y, z) to a new random location (x', y', z'), according to:

$$\begin{aligned} x' &= x + N(0, 2D\Delta t) \\ y' &= y + N(0, 2D\Delta t) \\ z' &= z + N(0, 2D\Delta t) \end{aligned} \quad (14)$$

Where, D=diffusion coefficient (μm^2/ms), Δt=simulation time step, $N(0,2D\Delta t)$=independent normal random variates, with mean μ=0, and standard deviation $\sigma = \sqrt{2D\Delta t}$. The total phase accumulated by the nth proton through time t is given by:

$$\varphi_n(t) = \sum_{j=1}^{t/\Delta t} \gamma\Delta B(\mathbf{p}_n(j\Delta t))\Delta t \quad (15)$$

Where, Δt = simulation time step, γ = proton gyromagnetic ratio (267.5×10^6 rad/Tesla), $\mathbf{p}_n(t)$ = position of nth proton at time t, $\Delta B(\mathbf{p})$ =magnetic field shift at position $\mathbf{p}$. The MR signal can then be estimated by summing the accumulated phase shift across the entire ensemble of N diffusing protons:

$$S(t) = \frac{1}{N}\sum_{n=1}^{N} e^{j\varphi_n(t)} \quad (16)$$

Simulations using an ensemble of random cylinders

To determine the computational accuracy of the FPM, we decided to assess the dependency of the gradient-echo (GE) and spin-echo (SE) relaxation rates i.e. ΔR2* and ΔR2, on vessel size, analogous to the approach used by Boxerman et al. (Boxerman, 1995b). For these simulations, we generated multiple ensembles of cylinders, each ensemble containing (approximately) fifty

randomly oriented cylinders that filled a 2% volume fraction of a cube, and varied the radius of the ensemble from 1–100μm while holding the fractional volume constant at 2%. Each simulation run included an ensemble of 1000 randomly placed protons, and since we generated sixty random ensembles for each vessel radius, this was equivalent to a simulation universe comprising of $60\times1000=6\times10^4$ protons. For the purposes of comparing the results of the FPM with those of Boxerman et al., we employed similar simulation parameters that included restricted diffusion with $D=1\times10^{-5}$ cm^2/s typical of the cerebral cortex (Chien et al., 1990), simulation time step $\Delta t=0.2ms$, $B_0=1.5T$, $\Delta\chi=1\times10^{-7}$ corresponding to an intravascular Gd-DTPA concentration of approximately 3.6mM (Weisskoff and Kiihne, 1992), GE TE=60ms and SE TE=100ms. For each ensemble, we determined the phase accumulated by the *n*th proton using Eq. 15, and the MR signal using Eq. 16. Since we generated 60 ensembles for each vessel radius, we first calculated the mean signal intensity for each radius, from which we calculated the associated relaxation change using:

$$\Delta R2^*, \Delta R2 = -\frac{\ln S(TE)}{TE} \tag{17}$$

Additionally, we determined the effect of different magnetic field strengths on the vessel size dependency of the GE and SE signals, by repeating the entire simulation for field strengths of 3T (GE TE=40ms, SE TE=80ms) and 4.7T (GE TE=10 and 60ms, SE TE=20 and 100ms).

Simulations using cerebrocortical microvessels as the model input

Finally, to demonstrate the effect of microvascular architecture on the MR signal, we computed the spin- and gradient-echo signals for a $70\times70\times70\mu m^3$ section of the cerebrocortical substrate (simulation parameters: $D=1\times10^{-5}$ cm^2/s, $\Delta t=0.2ms$, $B_0=1.5T$, $\Delta\chi=1\times10^{-7}$, GE TE=60ms and SE TE=100ms, grid size=256×256×256), and compared them to those obtained from an ensemble of random cylinders with identical simulation parameters. The physical dimensions of the ensemble of random cylinders was scaled to match those of the cerebrocortical network (i.e. fractional volume ~0.5%, average vessel radius=1.8μm).

RESULTS

Generating the Anatomical Data Structure

The reconstructed cerebrocortical capillary network is shown in Fig. 1b. The intricacy of the true vascular geometry is immediately apparent from this 3D volume rendering of the capillary network.

Computing the Magnetic Field Shift Due to the Vascular Structure

Fig. 2a shows a slice through the volume representing the vascular structure shown in Fig. 1b. One can see some blood vessels lie partly within the slice, while others penetrate the slice at more-or-less orthogonal angles. Fig. 2b shows a slice through the 3D Fourier transform of the vasculature, wherein one can observe that most of the signal content is at low spatial frequencies. Fig. 2c shows the magnetic field change arising from our infinitesimal *finite perturber*, barely visible at the center of the slice. Fig. 2d, shows a slice through the 3D Fourier transform of the finite perturber magnetic field; as expected, there is a high spatial frequency content. Fig. 2e displays the point-wise product of Figs. 2b and 2d. The inverse 3D Fourier transform of Fig. 2e is displayed in Fig. 2f, which also corresponds to the spatial convolution of Fig. 2a with Fig. 2c. Fig. 2f is the desired magnetic field shift due to the entire vascular structure. Finally, Fig. 1(c) illustrates the cerebrocortical network overlaid with a slice through the FPM-generated magnetic field map showing the magnetic field isolines.

Computing the Magnetic Field Shift for Simple Geometries to Validate the FPM

To validate the numerical accuracy of the FPM, we compared results obtained from the FPM with theoretical values of the magnetic field shift for various simple geometries. The columns in Fig. 3 show the effect of simulation grid size (i.e. number of finite perturbers) on the accuracy of the magnetic field calculated using the FPM, for the case of an infinitely long cylinder with the main magnetic field B_0, oriented along the z-axis as shown in Fig. 3a. **N.B.** in this and subsequent figures, the plotted magnetic field shift is "normalized", i.e.

$$\Delta B_{normalized} = \Delta B/(\Delta\chi B_0) \tag{18}$$

Fig. 3b shows a 3D surface plot of a slice in the XZ-plane through the magnetic field perturbation map due to the cylinder using a 64×64×64 simulation grid size. One can clearly distinguish the classic dipolar field pattern around the cylinder. Figs. 3c–e show the magnetic field profiles computed from theory along lines through the center of the cylinder, but parallel to the x, y and z-axes, respectively. Also shown for comparison are profiles along the same directions obtained using the FPM, and plots of the difference between the FPM and theory profiles for the simulation grid size of 64×64×64 (5120 finite perturbers, cell size=2μm^3). One can see that except for the discontinuity at the boundaries of the cylinder, there is excellent agreement between theory and FPM along all three axes. Figs. 3f–i show the magnetic field perturbation computed for the same scenario, but using a simulation grid size of 128×128×128 (40448 finite perturbers, cell size=1μm^3), and Figs. 3j–m using a simulation grid size of 256×256×256 (325632 finite perturbers, cell size=0.5μm^3), respectively. From these plots, one can again see the excellent agreement of the results from the FPM and those computed from theory. In addition one can also see a decrease in the computational error with increasing simulation grid size (i.e. increasing number of perturbers) as reflected by the decreasing area under the difference plot, especially at the boundaries of the cylinder. The "run time" for each of these simulations on a workstation with a dual core, 3.00GHz Xeon® processor with 2GB SDRAM was 19s, 31s and 110s, respectively. Similar plots of the numerical accuracy of the FPM for scenarios (b) and (c) (see *Computing the Magnetic Field Shift for Simple Geometries*) can be found in Supplemental Data.

Fig. 4 shows the projection onto a plane perpendicular to the axis of the cylinder in Fig. 3a of the simulated random diffusion trajectories for five protons, over a period of 60msec. This figure graphically illustrates how, over time, each proton experiences a different history of magnetic field perturbation. In Fig. 4a, proton diffusion is unrestricted, i.e. each proton is allowed to traverse the vessel wall. We can see that, in Fig. 4a, two of the protons have traversed the vessel wall multiple times. In Fig. 4b, we demonstrate the opposite case in which proton diffusion is restricted, i.e., no movement across the vessel wall is permitted. Thus, any proton that initially resides outside the vasculature will remain outside the vasculature; conversely, any proton that initially resides within the vasculature must remain inside the vasculature. Indeed, in Fig. 4b we see that one of the protons is forever "trapped" inside the blood vessel while another proton, initially located outside the blood vessel, is prevented from entering the blood vessel. As described above, this has profound implications for the resulting MR signal that is estimated by summing the accumulated phase shift across the entire ensemble of N diffusing protons in the simulation universe.

Simulations Using an Ensemble of Random Cylinders to Validate the FPM

To further validate the computational accuracy of the FPM, we decided to assess the dependency of the gradient-echo (GE) and spin-echo (SE) relaxation rates i.e. $\Delta R2^*$ and $\Delta R2$, on vessel size, analogous to the approach used by Boxerman et al. (Boxerman, 1995b). For these simulations, we generated multiple ensembles of (approximately) fifty randomly oriented cylinders that filled a 2% volume fraction of a cube, and varied the radius of the ensemble from

1–100μm while holding the fractional volume constant at 2%. Fig, 5a shows the FPM computed dependence of ΔR2* and ΔR2 on vessel size for B_0=1.5T, 2% fractional volume, and $\Delta\chi=1\times10^{-7}$. One can clearly see the excellent agreement of the FPM generated relaxation curves with those of Boxerman et al. in Fig. 5b [Reproduced with permission from (Boxerman, 1995b)], wherein the ΔR2 is seen to peak for microvessels while ΔR2*>ΔR2 for all radii, and plateaus for vessel radii > ~9μm. Fig. 5c illustrates the effect of increasing magnetic field strength (B_0) on the dependence of ΔR2* on vessel radius computed using the FPM. As field strength increases from 1.5T to 4.7T, even with the correspondingly shorter TEs typically employed at these higher fields, we observe a larger ΔR2* for the same dose of contrast agent (i.e. $\Delta\chi=1\times10^{-7}$). For comparison we can see that at 4.7T, for the same TE=60ms employed at 1.5T and the same contrast agent dose, we get a three to four-fold increase in relaxation rate. Fig. 5d illustrates the effect of increasing B_0 on the dependence of ΔR2 on vessel radius computed using the FPM. As field strength increases from 1.5T to 4.7T, even with the correspondingly shorter TEs typically employed at these higher fields we observe not only a larger ΔR2 for the same dose of contrast agent (i.e. $\Delta\chi=1\times10^{-7}$), but also a shift in peak sensitivity to smaller radii. For comparison one can see that at 4.7T, for the same TE=100ms employed at 1.5T and the same contrast agent dose, we not only get a three to four-fold increase in relaxation, but the peak vessel sensitivity shifts from ~6μm down to ~3μm. The "run time" for these simulations (18 radii×1000protons/radius×60ensembles=108×10^4 proton trajectories) was approximately 215mins.

Simulations using cerebrocortical microvessels as the model input

Fig. 6a shows a volume rendering of the section of the cerebrocortical capillary network employed in the GE and SE MR signal simulations. Fig. 6e shows a slice through the magnetic field perturbation map corresponding to the slice in Fig. 6c, wherein one can clearly visualize the dipolar field pattern around each capillary. Fig. 6f shows a 3D volume rendering of the ensemble of random cylinders with its physical dimensions scaled to match those of the cerebrocortical network (i.e. fractional volume ~0.5%, average vessel radius=1.8μm) for comparison. In Fig. 6j, a slice through the magnetic field perturbation map corresponding to the slice in Fig. 6h, one can not only visualize the dipolar field pattern around each cylinder, but can clearly discern the different 3D-spatial variations of the normalized magnetic field perturbation arising from the different vessel geometries shown in Figs. 6a and 6f. Finally, Fig. 7a, which plots the normalized GE and SE MR signals vs. time for the two cases illustrated in Fig. 6, unequivocally demonstrates the effect of microvascular geometry on both, the gradient- and spin-echo MRI signals. Collectively, these data demonstrate the feasibility of the FPM approach to compute the induced magnetic field changes and eventual MR signal evolution for arbitrarily shaped geometries, such as cerebrocortical vessels.

DISCUSSION

As mentioned earlier, several models have been developed to help understand the factors that contribute to susceptibility-induced MR signal change, and to quantify its association with the underlying microvascular geometry (Boxerman, 1995b; Fisel, 1991; Kiselev, 2001). However, the majority of these approaches have employed cylindrical perturbers (CP) to approximate the vascular architecture of the tissues being studied. As the analytical expressions for the magnetic field perturbations arising from CPs are available, it makes their use in simulations computationally convenient. However, traditional CP approaches have inherent assumptions that limit their applicability to pathological conditions (such as tumors). One assumption is that the magnetic field does not vary along the length of the vessels, and another is that inter-vessel separations are large. While the former assumption enables susceptibility effects to be simulated in 2D, since the induced field gradients are a function of the 3D geometry, any vessel geometry that departs from the cylindrical model would need to be simulated in 3D. The second

assumption simplifies the magnetic field calculations as the effect of overlapping magnetic fields around the vessels may be ignored at very large inter-vessel distances. However, this assumption may be inappropriate for tumor tissue – wherein although vessel density may be low, due to larger caliber tumor vessels (Pathak et al., 2001), the intervessel distances may not be negligible. Additionally, overlapping magnetic field gradients may become significant at high contrast agent doses, and the effect of overlapping magnetic field gradients may even dominate the eventual image contrast observed.

The recent demonstration that the microvessel architecture and possibly blood rheological factors are critical determinants of susceptibility-induced contrast (Pathak et al., 2003), especially for tumors with their characteristically abnormal vascular morphology, make the CP approximation employed by most models inappropriate in such cases. These results in conjunction with those from other studies (Kiselev, 2005) have created a crucial need for novel computational approaches that specifically take the *de facto* microvasculature into account while circumventing the shortcomings of traditional CP approaches, so that we might better understand the various factors that engender susceptibility-based contrast mechanisms. This is particularly true for the assessment of tumor angiogenesis using susceptibility-based contrast MRI (Pathak et al., 2003).

We have described a computational technique called the finite perturber method (FPM) that addresses several of the abovementioned issues. This technique allows us to estimate the susceptibility-induced MR signal for arbitrary microvascular geometries, such as those found in tumors. As demonstrated using a digitized version of a rat cerebrocortical capillary network, the FPM can compute the magnetic fields induced around the *de facto* microvasculature without necessitating any assumptions about microvessel geometry. In addition, these effects could be computed in the presence of overlapping fields from the different vessels, for a range of magnetic susceptibilities, in 3D.

Conventionally, one treats the magnetic field inside the spherical or cylindrical perturber as arising from the interface between continuous media. However, each spin and its immediate neighborhood cannot be considered a continuous distribution of magnetic field sources, because of which an important correction known as the Lorentz correction must be applied to the field equations for such perturbers. This correction defines a “Lorentz sphere” of influence around the spin due to the cancellation of the fields of nearby molecules (Haacke, 1999). An important advantage of the FPM, which computes the magnetic field shifts by summing the contributions of thousands of tiny cubes, is that it automatically incorporates the Lorentz correction.

The use of the FFT greatly improves the computational efficiency of the FPM in contrast to the earlier “nested-cube” type computational approaches, for example (Pathak, 2002). In addition, the FPM circumvents the disadvantages of classical numerical methods generally employed for calculating magnetic fields, such as the Finite Difference Method (FDM) and the Finite Element Method (FEM). While both these techniques are very general and have widespread applications, they suffer from severe limitations for the class of problem under consideration here. The FDM employs a uniform rectangular sampling simulation grid to define points at which a system of simultaneous finite difference equations are employed to solve Laplace’s equation for the scalar magnetic potential, from which the magnetic field shift (ΔB) can be eventually calculated (Binns, 1973). The disadvantages of the FDM approach are that a uniform rectangular simulation grid is a poor representation of the vasculature; there exists the numerical problem of subtracting nearly equal numbers i.e. $\Delta B=B–B_0$; also the Lorentz correction is not included. In contrast, the FEM represents space as a meshwork of finite elements, within each of which a polynomial form for the scalar magnetic potential is assumed, and solved to eventually extract ΔB (Binns, 1973). In addition to having drawbacks

similar to the FDM approach, the FEM approach has the difficulty of requiring automatic generation of a finite element mesh that adequately represents the fine detail of the vascular geometry.

We rigorously tested the numerical accuracy of our FPM approach using two independent approaches. In the first, we compared the magnetic field shifts computed with the FPM to those predicted by the theoretical solutions for two simple geometries, namely a cylinder and a sphere. We did this for spheres and cylinders with varying radii, and for a range of B_0 field strengths, and found exceptional agreement between the results from the analytical solutions and the FPM values, each time. Figs. 3f–i show the magnetic field perturbation computed for the same scenario, but using a simulation grid size of 128×128×128 (40448 finite perturbers for FV=2%), and Figs. 3j–m using a simulation grid size of 256×256×256 (325632 finite perturbers for FV=2%), respectively. From these plots, one can again see the excellent agreement of the results from the FPM and those computed from theory. We also observed a decrease in the computational error with increasing simulation grid size (i.e. increasing number of perturbers), especially at the boundaries of the cylinder. While there exists a trade-off between simulation grid size and computation time, the larger grid size could prove especially advantageous for representing subtle architectural changes in blood vessels that are typically observed in the early stages of tumor angiogenesis (Deane, 1981; Pathak et al., 2001), and is an ongoing area of investigation in our laboratory.

A couple of points about the FPM approach are worth emphasizing: first, the numerical results from the FPM demonstrated in Fig. 3 were obtained by summing the contributions from thousands of tiny cubes i.e. finite perturbers, and *not* by simply "plugging-in" values into the theoretical formula. Second, as can be seen from the plots in Fig. 3, the normal component of the ΔB field is *not* continuous at the perturber boundary, i.e. the FPM method *automatically* incorporates the Lorentz correction. This would *not* be the case for a naïve solution of Maxwell's equations, which assume homogeneity of the material substance inside the vasculature, as opposed to a *rigorous* solution of Maxwell's equations, which would allow for inhomogeneity of the medium, thereby incorporating the Lorentz correction. This is not a trivial matter, and we believe that the difficulty of implementing the rigorous solution of Maxwell's equations makes other methods, such as the finite difference method and the finite element method, impractical for the current application, and was the primary motivation for developing the finite perturber method.

We also validated the computational accuracy of the FPM by assessing the dependency of the gradient-echo (GE) and spin-echo (SE) relaxation rates i.e. $\Delta R2^*$ and $\Delta R2$, on vessel size, using simulation parameters identical to those employed by Boxerman et al. (Boxerman, 1995b). Again, we observed excellent agreement of the FPM-generated relaxation curves with those of Boxerman et al. (Figs. 5a–b). We also simulated the effect of increasing magnetic field strength (B_0) on the dependence of $\Delta R2^*$ (and $\Delta R2$) on vessel radius, using values for B_0 and TE typical of clinical magnets. For the range of TEs employed and for the same dose of contrast agent (i.e. $\Delta\chi=1\times10^{-7}$), we observed an increase in $\Delta R2^*$ as B_0 increased from 1.5T to 4.7T. For example (Fig. 5c) we can see that for the same TE=60ms and contrast agent dose, we get a three to fourfold increase in $\Delta R2^*$ at 4.7T relative to 1.5T, thereby providing greater SNR for relative cerebral blood volume (rCBV) measurements at higher field strengths. However, as field strength increases from 1.5T to 4.7T, for the range of TEs employed we observed not only an increase in $\Delta R2$ for a constant dose of contrast agent (i.e. $\Delta\chi=1\times10^{-7}$), but also a shift in peak sensitivity to smaller radii. For example (Fig. 5c) we can see that for the same TE=100ms and contrast agent dose, we not only get a three to four-fold increase in $\Delta R2$, but the peak vessel sensitivity shifts from ~6μm down to ~3μm between 1.5T and 4.7T, thereby providing greater microvascular sensitivity for SE protocols. A similar two-fold effect on $\Delta R2$ was also observed by Boxerman et al. when they increased the strength of the perturbation by

increasing $\Delta\chi$ while keeping B_0 constant, an explanation for which was provided by Weisskoff et al. using scaling laws (Weisskoff, 1994). The same scaling laws are applicable to our case wherein the magnetic perturbation was increased by increasing B_0 while keeping $\Delta\chi$ constant. For a two-fold increase in the strength of the perturbation (from 1.5T to 3T, for example) these scaling laws predict a quadratic dependence of relaxivity on B_0 for small-sized vessels (1–3μm), linear dependence near the peak of the relaxation curve (4–6μm), and a sub-linear dependence in the large-sized vessel range (>10μm), just as our simulations predict. Details regarding the derivation of these scaling laws from the Bloch-Torrey equations can be found in (Weisskoff, 1994). This independent validation of the FPM is all the more significant since Boxerman et al. employed an entirely different computational technique to simulate the biophysics of the MR signal. Specifically, they employed an iterative, Monte-Carlo approach using the equations for infinitely long cylindrical perturbers (Eq. 9).

Limitations of the FPM

As explained in the Methods section, the FPM uses the Fast Fourier transform (FFT) to calculate the spatial convolution of the vascular structure with the finite perturber magnetic field distortion. One limitation of this method is that the FFT convolution is a "circular-convolution" i.e., the result of the convolution is the same as if the underlying vascular structure were spatially periodic. In effect, the "top" of the simulation space is glued to the "bottom" of the simulation space; the "left" edge is attached to the "right" edge; and the "front" of the simulation space coincides with the "rear". This is illustrated in Figs. 7b–c. In Fig. 7b, the vasculature is modeled by a single, long cylinder that crosses the simulation space at an oblique angle. In Fig. 7c is plotted the magnetic field distortion arising from this vessel, using the FPM. Comparing Figs. 7b and 7c, we see that calculated field differs from what we would expect for an infinite cylinder. This is not the field pattern for an infinite cylinder, but for a cylinder that is truncated and spatially periodic. In the left panel of Fig. 7c, the calculated magnetic field along the top edge of the simulation space corresponds to the vasculature that is present along the bottom edge, and vice versa. Therefore, caution must be exercised to avoid "boundary effects". A possible solution is to "zero-pad" the vascular dataset, to keep the vasculature away from the simulation boundary. However, this is not a perfect solution either, as the true "real-world" vasculature usually extends well beyond the boundary of the simulation space. Thus, such "boundary effects" will always pose a problem for *any* numerical method.

Finally, the results presented herein demonstrate the versatility of the FPM for simulating an array of susceptibility-based contrast mechanisms. In addition to the BOLD contrast mechanism, we are primarily interested in the effect of vascular remodeling that accompanies tumor angiogenesis and anti-angiogenic therapy, on susceptibility-based contrast. We are currently in the process of investigating the effects of an array of physiological variables on the biophysics of susceptibility-based contrast within the context of brain tumors.

CONCLUSIONS

Here, for the first time we have successfully demonstrated both the numerical accuracy and the feasibility of a novel computational and simulation technique for estimating the susceptibility-induced MR signal for *arbitrary* microvascular geometries. Further, our technique allows us to visualize these effects in 3D and in exquisite detail. The excellent agreement of the FPM with theory indicates that it could greatly advance our understanding of susceptibility-based contrast mechanisms, particularly within the context of tumor angiogenesis.

SUPPLEMENTARY DATA

Refer to Web version on PubMed Central for supplementary material.

Acknowledgements

The authors would like to thank Dr. Tony Hudetz for all his assistance with the cerebrocortical vascular network.

Research was supported by NIH P50CA103175 – Career Development Award (APP), NIH/NCI R01CA82500-01A1 (KMS).

References

Aronen HJ, Gazit IE, Louis DN, Buchbinder BR, Pardo FS, Weisskoff RM, Harsh GR, Cosgrove GR, Halpern EF, Hochberg FH, Rosen BR. Cerebral Blood Volume Maps of Gliomas: Comparison with Tumor Grade and Histological Findings. Radiology 1994;191:41–51. [PubMed: 8134596]

Bandettini PA, Wong EC. The effects of biophysical and physiologic parameters on brain activation - induced R2* and R2 changes: simulations using a deterministic diffusion model. Int J of Imaging Systems and Technology 1995;6:133–152.

Bandettini PA, Wong EC. The Effects of Biophysical and Physiologic Parameters on Brain Activation-Induced R2* and R2 Changes: Simulations Using a Deterministic Diffusion Model. Int J Imaging Syst Tech 1995;6:133–152.

Belliveau JW, Kennedy DN, McKinstry RC, Buchbinder BR, Weisskoff RM, Cohen MS, Vevea JM, Brady TJ, Rosen BR. Functional mapping of the human visual cortex by magnetic resonance imaging. Science 1991;254:716–719. [PubMed: 1948051]

Binns, KJ.; Lawrenson, PJ. Analysis and Computation of Electric and Magnetic Field problems. Pergamon Press Ltd; New York: 1973.

Boxerman JL, Bandettini PA, Kwong KK, Baker JR, Davis TL, Rosen BR, Weisskoff RM. The Intravascular Contribution of fMRI Signal Change: Monte Carlo Modeling and Diffusion Weighted Studies In Vivo. Mag Reson Med 1995a;34:4–10.

Boxerman JL, Hamberg LM, Rosen BR, Weisskoff RM. MR Contrast Due to Intravascular Magnetic Susceptibility Perturbations. Mag Reson Med 1995b;34:555–566.

Boxerman, JLWR.; Hoppel, BE.; Rosen, BR. MR Contrast Due to Microscopically Heterogeneous Magnetic Susceptibility: Cylindrical Geometry. 1st Annual Meeting, Society of Magnetic Resonance in Medicine; New York. 1993. p. 389

Chien D, Buxton RB, Kwong KK, Brady TJ, Rosen BR. MR diffusion imaging of the human brain. J Comput Assist Tomogr 1990;14:514–520. [PubMed: 2370348]

Deane BR, Lantos PL. The Vasculature of Experimental Brain Tumors - Part 2: A quantitative Assessment of Morphological Abnormalities. J Neurological Science 1981;49:67–77.

Donahue KM, Krouwer HG, Rand SD, Pathak AP, Marszalkowski CS, Censky SC, Prost RW. Utility of simultaneously acquired gradient-echo and spin-echo cerebral blood volume and morphology maps in brain tumor patients. Magn Reson Med 2000;43:845–853. [PubMed: 10861879]

Fisel CR, Ackerman JL, Buxton RB, Garrido L, Belliveau JW, Rosen RB, Brady TJ. MR Contrast Due to Microscopically Heterogeneous Magnetic Susceptibility: Numerical Simulations and Applications to Cerebral Physiology. Mag Reson Med 1991;17:336–347.

Haacke, EM.; Brown, RW.; Thompson, MR.; Venkatesan, R. Magnetic Resonance Imaging: Physical Principles and Sequence Design. Wiley-Liss; New York: 1999. Magnetic Properties of Tissues: Theory and Measurement; p. 741-779.

Hudetz AG, Green AS, Fehrer G, Kneuse DK, Cowley AW. Imaging System for Three-Dimensional Mapping of Cerebrocortical Capillary Networks *In Vivo*. Microvascular Res 1993;46:293–309.

Jenkinson M, Wilson JL, Jezzard P. Perturbation method for magnetic field calculations of nonconductive objects. Magn Reson Med 2004;52:471–477. [PubMed: 15334564]

Kennan RP. Intravascular Susceptibility Contrast Mechanisms in Tissues. Mag Reson Med 1994;31:9–21.

Kiselev VG. On the Theoretical Basis of Perfusion Measurements by Dynamic Susceptibility Contrast MRI. Mag Reson Med 2001;46:1113–1122.

Kiselev VG. Transverse relaxation effect of MRI contrast agents: a crucial issue for quantitative measurements of cerebral perfusion. J Magn Reson Imaging 2005;22:693–696. [PubMed: 16261568]

Koch KM, Papademetris X, Rothman DL, de Graaf RA. Rapid calculations of susceptibility-induced magnetostatic field perturbations for in vivo magnetic resonance. Phys Med Biol 2006;51:6381–6402. [PubMed: 17148824]

Landau, LD.; Lifshitz, EM. Electrodynamics of Continuous Media. 2. Pergamon; Oxford: 1984.

Li L, Leigh JS. Quantifying arbitrary magnetic susceptibility distributions with MR. Magn Reson Med 2004;51:1077–1082. [PubMed: 15122694]

Maeda M, Itoh S, Kimura H, Iwasaki T, Hayashi N, Yamamoto K, Ishii Y, Kubota T. Tumor Vascularity in the Brain: Evaluation with Dynamic Susceptibility-Contrast MR Imaging. Radiology 1993;189:233–238. [PubMed: 8372199]

Ogawa S. MRI of Blood Vessels at High Fields: In Vivo and In Vitro Measurements and Image Simulation. Mag Reson Med 1990;16:9–18.

Pathak A, Schmainda K, Ward B, Linderman J, Rebro KJ, Greene AS. MR-derived cerebral blood volume maps: issues regarding histological validation and assessment of tumor angiogenesis. Magn Reson Med 2001;46:735–747. [PubMed: 11590650]

Pathak AP, Rand SD, Schmainda KM. The effect of brain tumor angiogenesis on the in vivo relationship between the gradient-echo relaxation rate change (DeltaR2*) and contrast agent (MION) dose. J Magn Reson Imaging 2003;18:397–403. [PubMed: 14508775]

Pathak, AP.; Ward, BD.; Hudetz, AG.; Schmainda, KM. A Novel Technique for Estimating the Susceptibility-Induced MR Signal For Arbitrary Microvascular Geometries: The Finite Perturber Method. ISMRM, 10th Annual Mtg; Honolulu, Hawaii. 2002. p. 1331

Rosen BR. Perfusion Imaging with NMR Contrast Agents. Mag Reson Med 1990;14:249–265.

Rosen BR. Susceptibility Contrast Imaging of Cerebral Blood Volume: Human Experience. Mag Reson Med 1991a;22:293–299.

Rosen BR, Belliveau JW, Buchbinder BR, McKinstry RC, Porkka LM, Kennedy DN, Neuder MS, Fisel CR, Aronen HJ, Kwong KK, Weisskoff RM, Cohen MS, Brady TJ. Contrast Agents and Cerebral Hemodynamics. Mag Reson Med 1991b;19:285–292.

Shen T, Weissleder R, Papisov M, Bogdanov A Jr, Brady TJ. Monocrystalline Iron Oxide Nanoparticles (MION): Physiochemical Properties. Mag Reson Med 1993;29:599–604.

Weisskoff RM, Kiihne S. MRI susceptometry: image-based measurement of absolute susceptibility of MR contrast agents and human blood. Magn Reson Med 1992;24:375–383. [PubMed: 1569876]

Weisskoff RM, Zuo CS, Boxerman JL, Rosen BR. Microscopic Susceptibility Variation and Transverse Relaxation: Theory and Experiment. Mag Reson Med 1994;31:601–610.

Yablonskiy DA. Theory of NMR Signal Behavior in Magnetically Inhomogeneous Tissues: The Static Dephasing Regime. Mag Reson Med 1994;32:749–763.

Zierler KL. Theoretical Basis of Indicator-Dilution Methods for Measuring Flow and Volume. Circulation Res 1962 March;X:393–407.

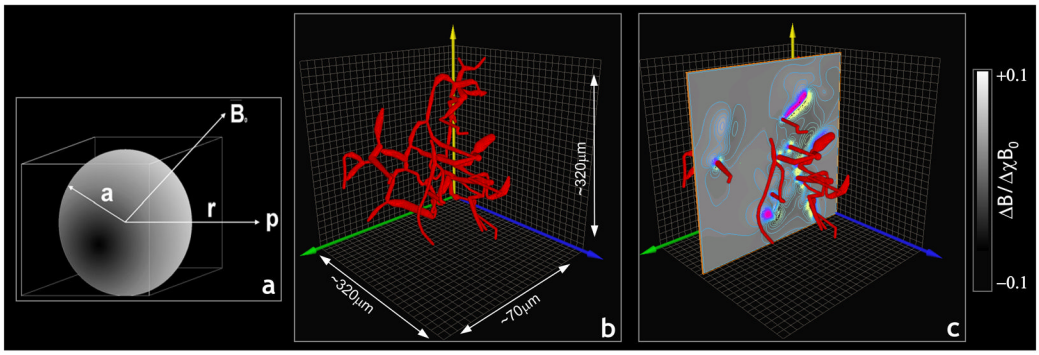

Fig 1.

(a) Schematic illustrating the geometry for calculating the magnetic field perturbation due to a tiny cube (the "finite perturber"). We estimate the field induced around the cube by considering a sphere of radius '*a*', embedded in a cube of side '*2a*'. A test point **p**(x,y,z,) is located at a distance '*r*' from the center of the perturber placed in field B_0. (b) 3D volume rendering of a rat cerebrocortical capillary network. (c) Volume rendered cortical substrate in (b) overlaid with a slice through the FPM generated magnetic field map showing the magnetic field isolines.

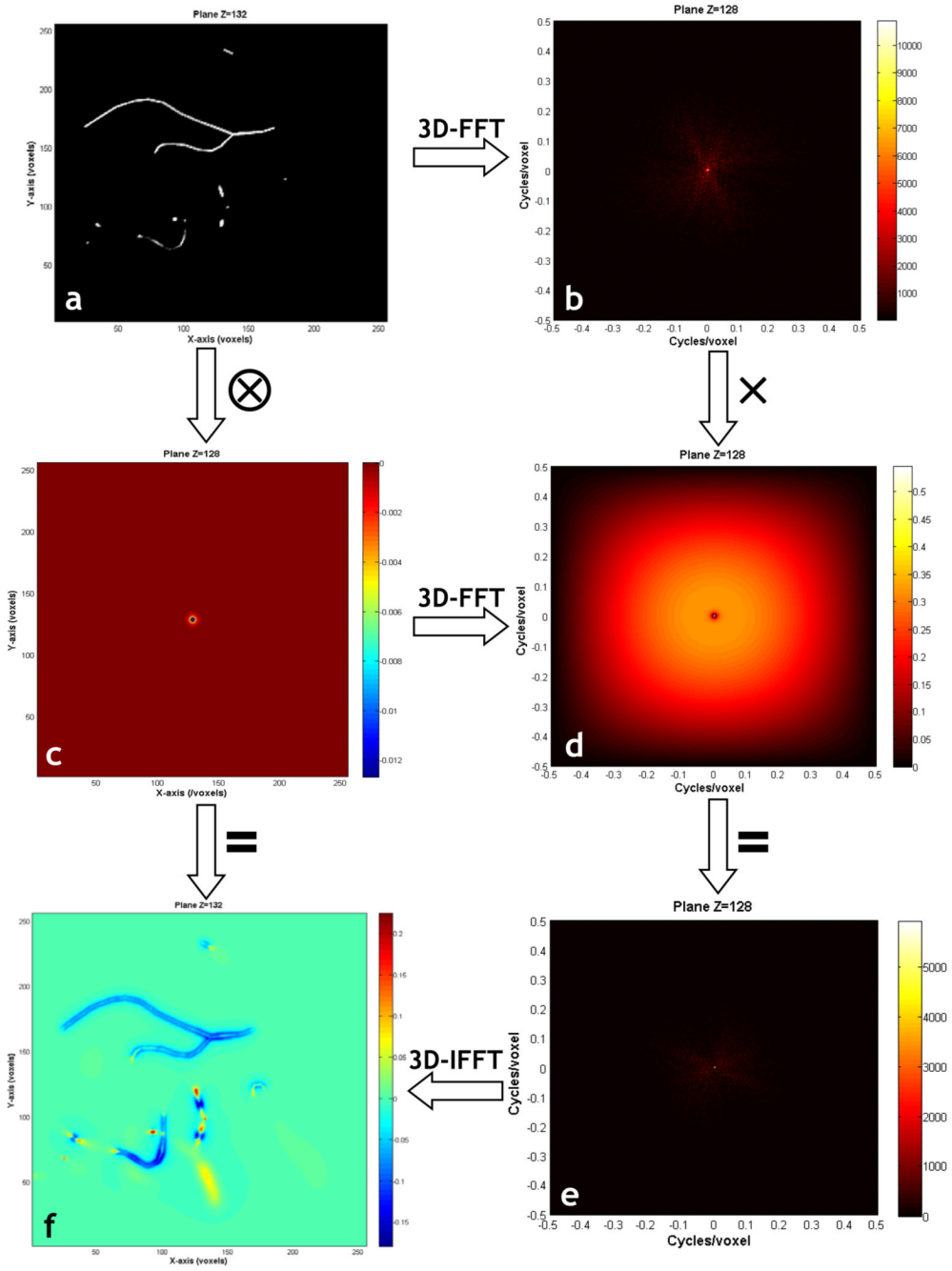

Fig 2.

This figure illustrates the steps involved in computing the magnetic field shifts due to the input vasculature using the FPM: (a) 2D slice through the vasculature. (b) 2D slice through the 3D Fourier transform of (a). (c) 2D slice through the normalized ($\Delta B_{normalized}$) finite perturber magnetic field. (d) 2D slice through the 3D Fourier transform of (c). Point-wise multiplication of (b) and (d) in the Fourier domain yields (e). (f) is a 2D slice through the 3D inverse Fourier transform of (e), and is also a result of the convolution of (a) and (c). (f) Is the sought after normalized ($\Delta B_{normalized}$) magnetic field shift due to the arbitrarily shaped vascular tree.

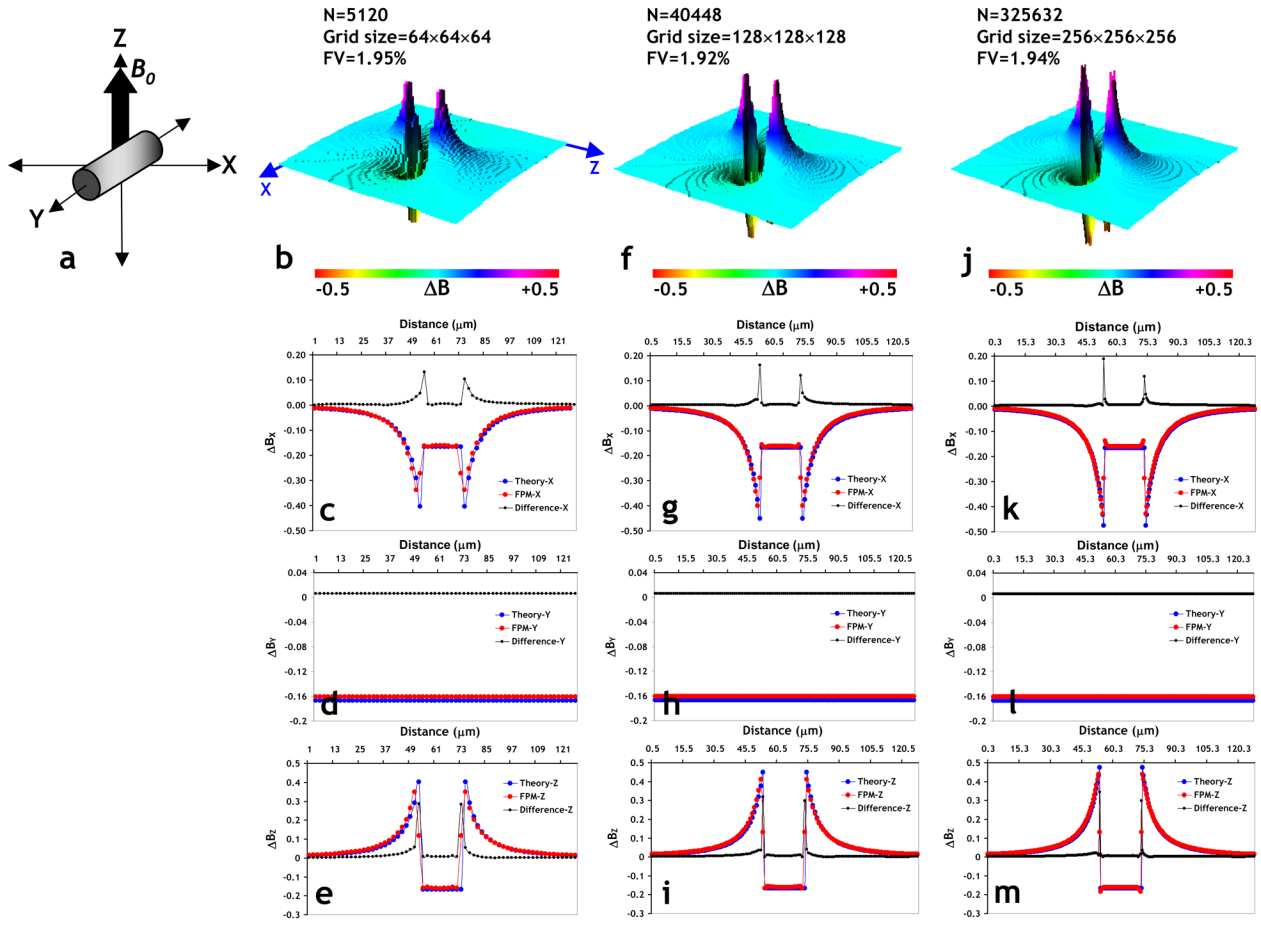

Fig 3.

(a) Schematic illustrating the orientation of an infinitely long cylinder (2% fractional volume, $\Delta\chi=3\times10^{-8}$) relative to the main magnetic field B_0=1.5T, employed to check the effect of simulation grid size on the accuracy of the magnetic field calculated using the FPM. (b) Surface plot of a slice in the XZ-plane through the magnetic field perturbation map due to the cylinder in (a) using a 64×64×64 simulation grid size. One can clearly distinguish the classic dipolar field pattern around the cylinder. Plots of the magnetic field profile predicted by theory (blue) versus those computed using the FPM (red), and the difference between the two (black) plotted along the x-axis (c), y-axis (d), and z-axis (e), respectively. The number of finite perturbers required to fill the cylinder was 5120. (f–i) are the same results for a simulation grid size of 128×128×128 (40448 finite perturbers required), and (j–m) for a simulation grid size of 256×256×256 (325632 finite perturbers required), respectively. From these plots one can clearly see the excellent agreement of the results from the FPM and those predicted by theory even at the coarsest simulation grid size. In addition, one can also see a decrease in the computational error with increasing simulation grid size, as reflected by the decreasing area under the difference plot. This is especially evident at the surface of the cylinder i.e. at the interface of the cylinder and background.

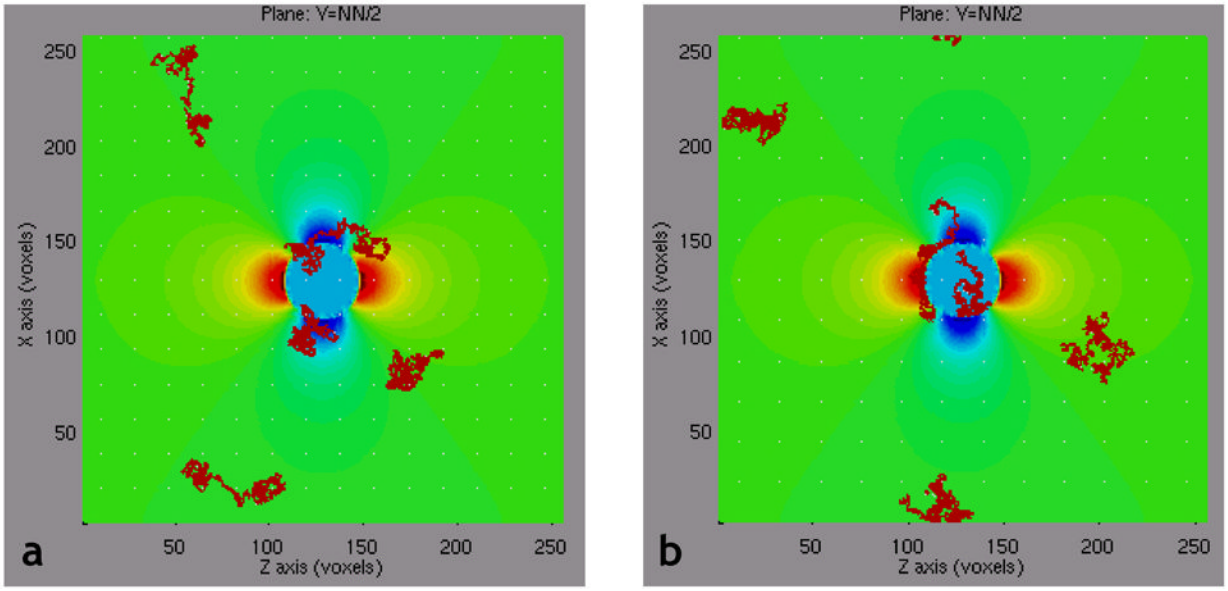

Fig 4.

Projection of five 3D proton diffusion paths onto a slice through magnetic field perturbation due to the cylinder in Fig. 3a, for: (a) the unrestricted proton diffusion case, i.e. proton allowed to traverse the vessel boundary, and (b) the restricted proton diffusion case, i.e. proton is not allowed to traverse the vessel boundary.

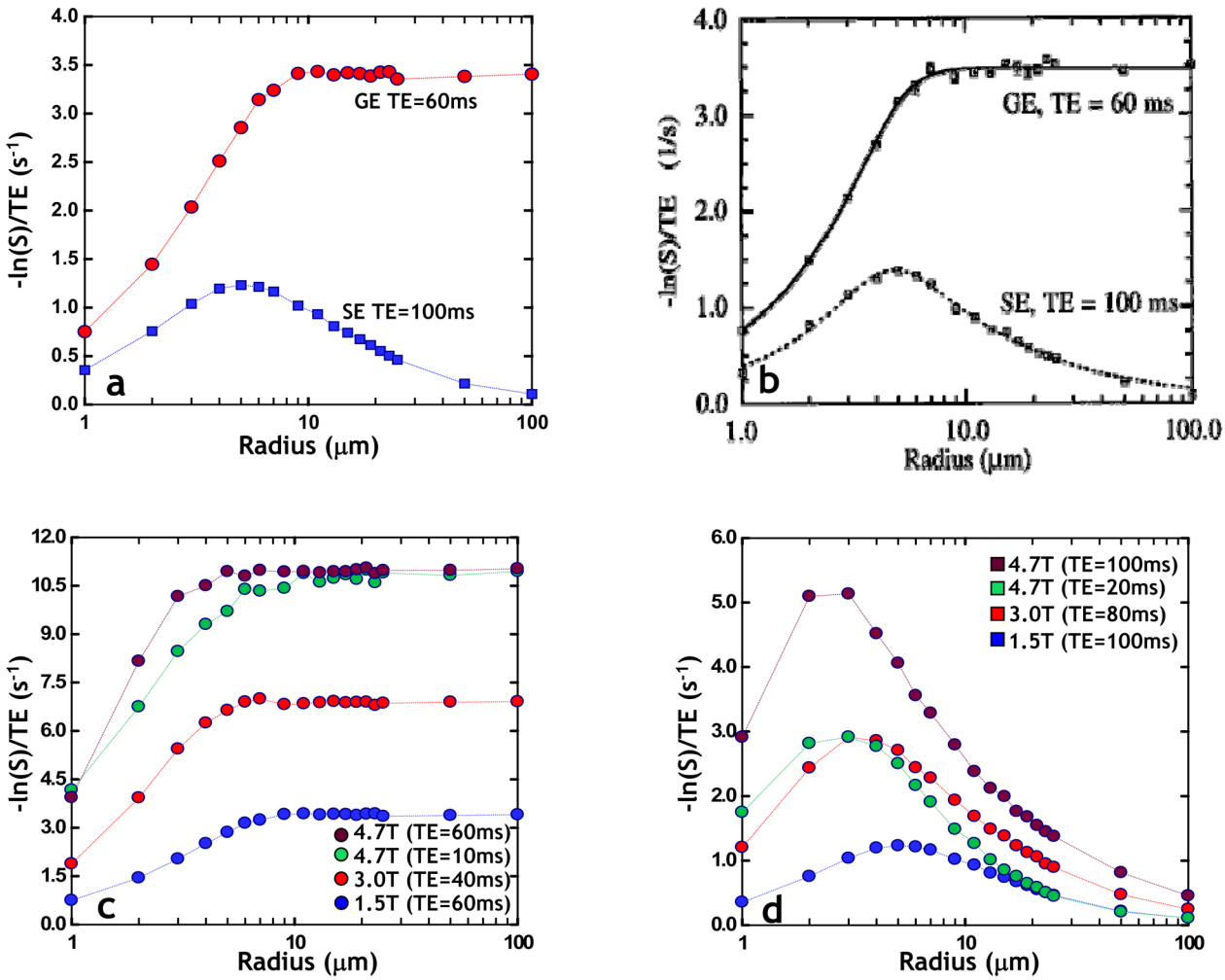

Fig 5.

(a) FPM computed dependence of ΔR2* and ΔR2 on vessel size for B_0=1.5T, 2% fractional volume, and $\Delta\chi=1\times10^{-7}$. One can see excellent agreement of the FPM generated curves with those of Boxerman et al. shown in (b) [Reproduced with permission from (Boxerman, 1995b)], wherein the ΔR2 peaks for microvessels while the ΔR2*>ΔR2 for all radii, and plateaus for vessel radii > ~9μm. (c) The effect of magnetic field strength (B_0) on the dependence of ΔR2* on vessel radius computed using the FPM. (d) The effect of magnetic field strength (B_0) on the dependence of ΔR2 on vessel radius computed using the FPM.

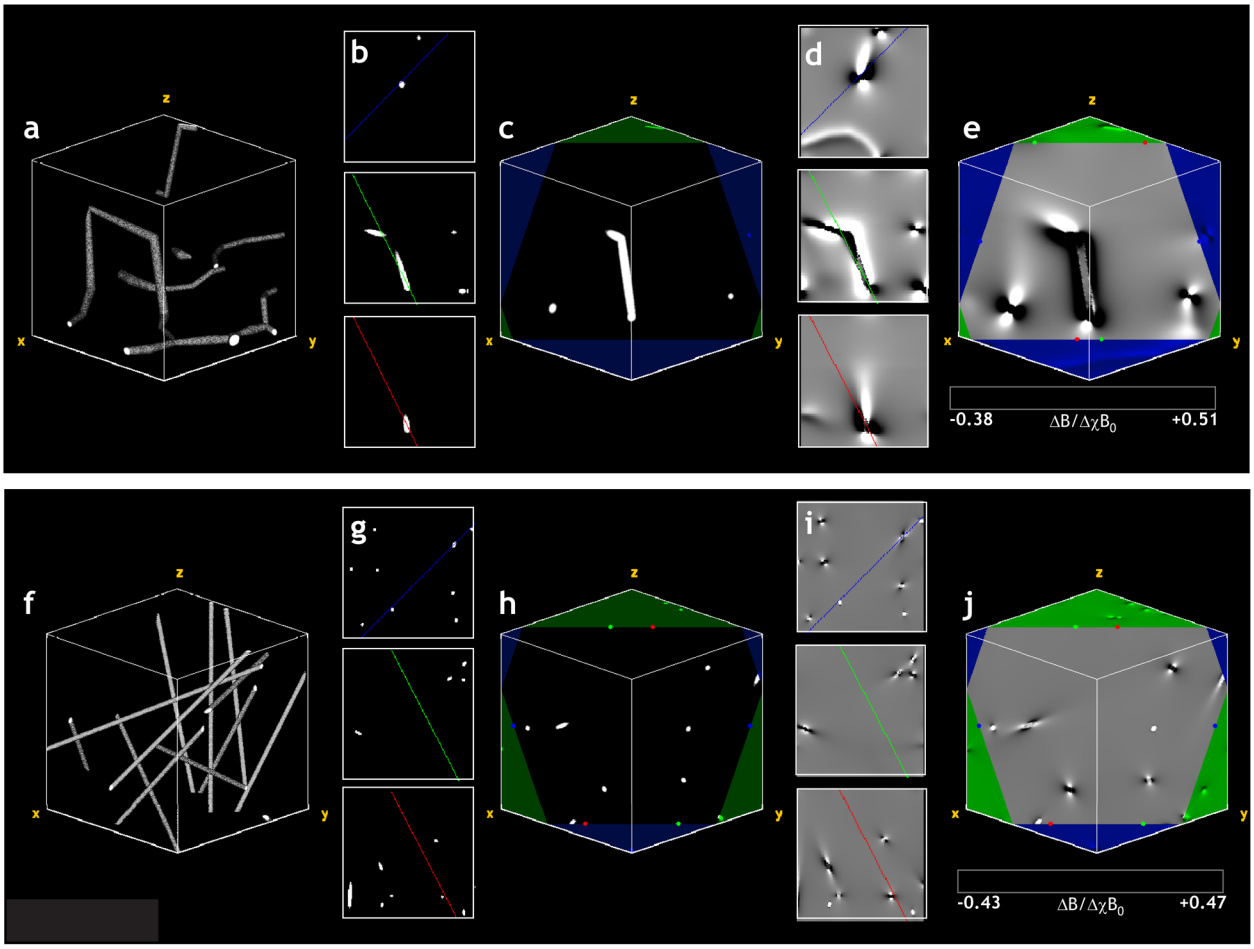

Fig 6.

(a) 3D volume rendering of the section of the cerebrocortical capillary network employed in the GE and SE MR signal simulations. (b) Three orthogonal center planes of the volume in (a) with colored lines indicating the intersection of the displayed slice and the three orthogonal center planes of the volume. (c) A slice through the volume in (a) with the borders of the volume displayed in green. The red, green and blue colored markers indicate the start and end positions of the lines in the planar views shown in (b). (d) Three orthogonal center planes of the *normalized* magnetic field perturbation map corresponding to the capillary network in (a). (e) A slice through the magnetic field perturbation map corresponding to the slice in (c). One can clearly visualize the dipolar field pattern around each capillary. (f) 3D volume rendering of the ensemble of random cylinders employed in the GE and SE MR signal simulations, with its physical dimensions scaled to match those of the cerebrocortical network (i.e. fractional volume ~0.5%, average vessel radius=1.8μm). (g) Three orthogonal center planes of the volume in (f) with colored lines indicating the intersection of the displayed slice and the three orthogonal center planes of the volume. (h) A slice through the volume in (f) with the borders of the volume displayed in green. The red, green and blue colored markers indicate the start and end positions of the lines in the planar views shown in (g). (i) Three orthogonal center planes of the *normalized* magnetic field perturbation map corresponding to the cylinders in (f). (j) A slice through the magnetic field perturbation map corresponding to the slice in (c). One can visualize the dipolar field pattern around each cylinder, and see differences in 3D-spatial variations of the magnetic field perturbations between geometries (e) and (f).

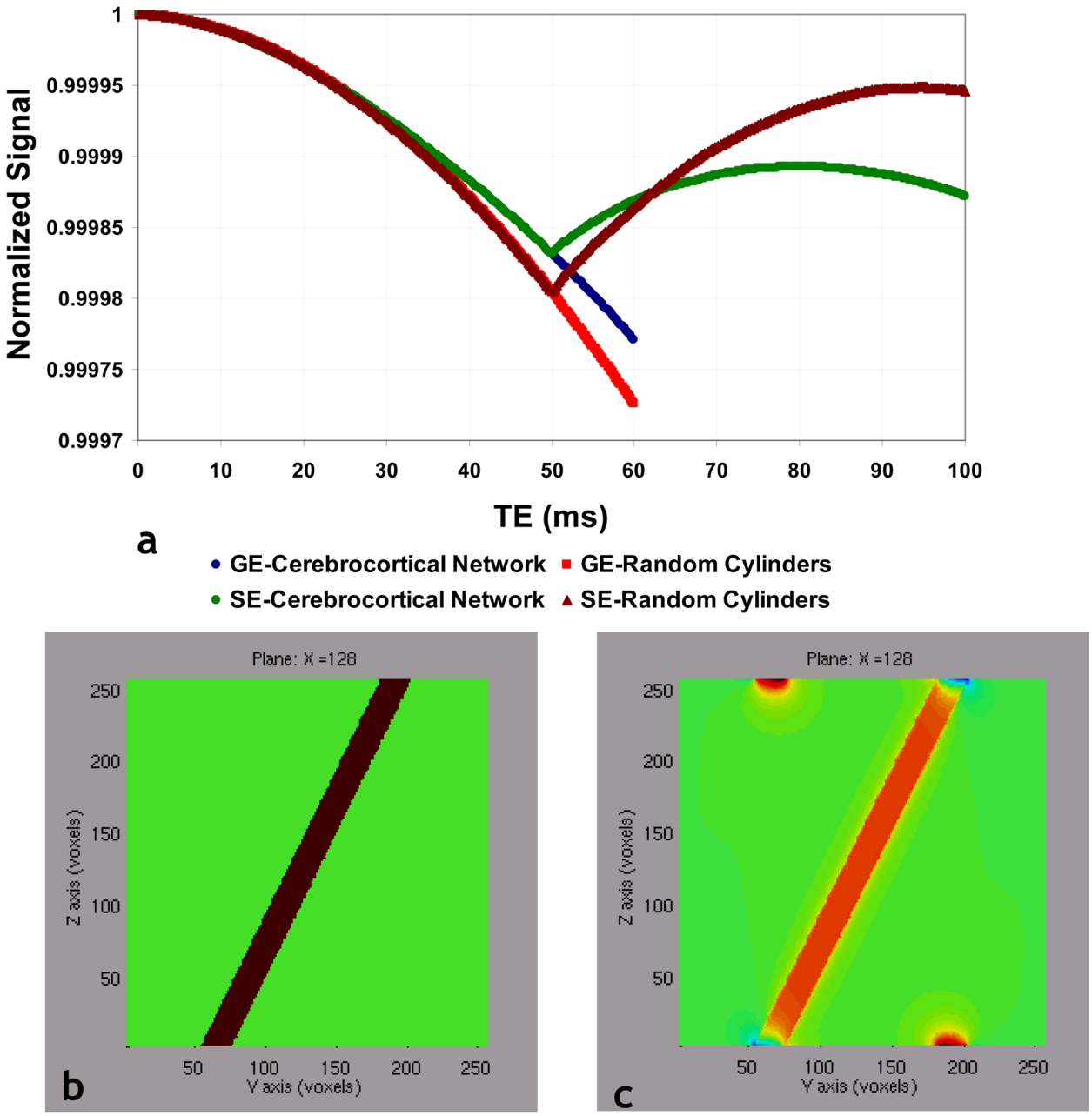

Fig 7.

(a) Normalized GE and SE signals computed for the vascular substrates shown in Fig. 6. (b) Vasculature modeled by a single, long cylinder that crosses the simulation space at an oblique angle. (c) Plot of the magnetic field distortion arising from this vessel computed using the FPM. Comparing (b) and (c), we see that calculated field differs from what we would expect for an infinite cylinder. In (c) the calculated magnetic field along the top edge of the simulation space corresponds to the vasculature that is present along the bottom edge, and vice versa.